Combined enhanced fluorescence and label-free biomolecular detection with a photonic crystal surface

Patrick C. Mathias, Nikhil Ganesh, Leo L. Chan, and Brian T. Cunningham

A 2D photonic crystal surface with a different period in each lateral direction is demonstrated to detect biomolecules using two distinct sensing modalities. The sensing mechanisms both rely on the generation of a resonant reflection peak at one of two specific wavelengths, depending on the polarization of light that is incident on the photonic crystal. One polarization results in a resonant reflection peak in the visible spectrum to coincide with the excitation wavelength of a fluorophore, while the orthogonal polarization results in a resonant reflection peak at an infrared wavelength which is used for label-free detection of adsorbed biomolecules. The photonic crystal resonance for fluorescence excitation causes enhanced near fields at the structure surface, resulting in increased signal from fluorophores within 100 nm of the device surface. Label-free detection is performed by illuminating the photonic crystal with white light and monitoring shifts in the peak reflected wavelength of the infrared resonance with a high-resolution imaging detection instrument. Rigorous coupled-wave analysis was used to determine optimal dimensions for the photonic crystal structure, and devices were fabricated using a polymer-based nanoreplica molding approach. Fluorescence-based and label-free detection were demonstrated using arrays of spots of dye-conjugated streptavidin. Quantification of the fluorescent signal showed that the fluorescence output from protein spots on the photonic crystal was increased by up to a factor of 35, and deposited spots were also imaged in the label-free detection mode.

OCIS codes: 170.2520, 230.1950.

1. Introduction

Detection through the use of fluorescent labels has been one of the most widespread methods for quantifying and visualizing biomolecules for the past 25 years, and has been applied to innumerable assay protocols. In many of these protocols an instrument such as a fluorescence microscope or a fluorescence laser scanner is used to provide excitation of the fluorophore and detection of the emission of a labeled analyte on a solid surface, such as a glass microscope slide. High resolution imaging of cells and high throughput and large-area affinity microarray assays for DNA or proteins are among the applications for detection of fluorescent labels.[1,2]

Recently, the ability to amplify the signal–noise output of common fluorophores has been demonstrated by substitution of the passive glass surface with a specially designed optical resonator surface.[3,4] A submicrometer periodic structure is designed to enhance near fields during illumination that are strongly confined within the device at a wavelength that coincides with the excitation wavelength of the fluorophore, resulting in enhanced fluorescence (EF). Through the design of these devices that strictly limit the lateral propagation of coupled light, sensitivity enhancements of 2 orders of magnitude have been achieved relative to common epifluorescence that allows the imaging of DNA microarrays at high resolution. One important application of EF is in the field of gene expression analysis, where the enhanced sensitivity permits the detection of genes at lower concentrations than were previously possible.

Since the introduction of surface plasmon resonance (SPR), label-free (LF) optical detection of biomolecules has also found widespread acceptance in life science research.[5–7] Optical biosensors measure the adsorption of biomolecules to a transducer surface directly through the dielectric permittivity of the analyte, and thus are useful for detection of molecules that cannot be labeled effectively without altering their function. While optical biosensors generally have lower sensitivity performance than fluorescence

The authors are with the Nano Sensors Group, Department of Electrical and Computer Engineering, University of Illinois at Urbana-Champaign, Micro and Nanotechnology Laboratory, 208 N. Wright Street, Urbana, Illinois 61801, USA. B. T. Cunningham's e-mail address is bcunning@uiuc.edu.

Received 16 August 2006; revised 20 November 2006; accepted 14 December 2006; posted 20 December 2006 (Doc. ID 74107); published 3 April 2007.

0003-6935/07/122351-10$15.00/0

detection, they are typically capable of <5 pg/mm^2 mass density resolution, corresponding to approximately 50 protein molecules of 50 kDa molecular weight within a 1 μm $\times$ 1 μm area.[8] While many optical biosensor transducers have been demonstrated, only a few are capable of gathering high-resolution images of biomolecular density, and fewer still are capable of imaging over substantial surface areas. Of these, only photonic crystal (PC) optical biosensors and associated imaging detection instruments have demonstrated <1 pg/mm^2 mass resolution with <10 μm $\times$ 10 μm pixel resolution over surface areas that encompass entire microplates or microarray slides.[9]

Like submicrometer periodic structured EF devices, PC biosensors utilize a subwavelength periodic dielectric surface structure that results in strong resonant reflection at a narrow band of wavelengths. LF detection is achieved by illuminating the PC structure with a white-light source and detecting the narrow band of reflected wavelengths with a spectrometer. Biomolecule adsorption on the PC surface results in a shift of the peak wavelength value (PWV), which is the wavelength at the point of maximum reflection, to longer wavelengths on a pixel-by-pixel basis with a detection instrument that incorporates an imaging spectrometer.[10] Although the PC biosensor structure requires fabrication of features with dimensions <0.5 μm, it can be fabricated inexpensively over large surface areas with plastic-based materials through a nanoreplica molding process. The proper operation of both periodic EF structures and PC biosensor structures requires a periodic surface structure consisting of a low refractive index material (such as glass or plastic) that is coated with a thin layer of high refractive index material (such as Si_3N_4, TiO_2, or Ta_2O_5).

The ability to combine EF images with LF adsorption detection on a single PC would offer enormous benefits for a wide range of assays that are commonly performed. For example, the measurement of immobilized DNA microarray spots for spot density and spatial uniformity could be performed in a LF mode as a means for performing calibration and quality control during the detection of fluorescent-labeled DNA. The LF detection mode may also be used for detection of surface chemistry adsorption, blocking reagents, and small molecules that are not typically labeled by fluorophores, and for integrated secondary verification of tagged molecules by an independent modality.

In this work we demonstrate the combination of EF and LF PC biodetection on a surface that integrates both functions. The surface is a 2D PC that is designed with different periods along orthogonal directions, so the resonant coupling of two independent wavelengths can be achieved for separate electric field polarizations of incident light. The EF resonant coupling is designed to coincide with the 635 nm excitation wavelength of the fluorophore Cyanine-5 (Cy5), while the LF resonant coupling is designed to occur at 850 nm. This paper will describe the computational modeling that is used to design the 2D PC–EF structure, the fabrication of the structure through construction of a silicon mold template and nanoreplica molding into plastic, the characterization of the resonance performance of the structure, and the detection demonstration of Cy5-labeled streptavidin microarray spots by the EF and LF biosensor methods. The EF mode demonstrates approximately 35$\times$ higher fluorescence output compared with array spots that are not deposited on the structure using a conventional microarray laser scanner.

2. Device Design

Guided-mode resonance filters (GMRFs) are a recently developed class of PC structures with the capability for resonant coupling of a particular wavelength with approximately 100% reflection efficiency while allowing other wavelengths to transmit through the structure.[11,12] At the resonant wavelength, light is coupled to leaky modes that constructively interfere with the backward zeroth diffracted order and destructively interfere with the forward zeroth diffracted order. Energy is localized in this interaction, and a high electric field magnitude is generated within the dielectric layer and extends to the device surface.[13,14] Several types of GMRF structures have been demonstrated, including 1D and 2D periodic surface structures for applications including narrowband optical filters[15,16] and LF optical biosensors.[10] Such structures are advantageous for their narrowband resonant behavior and simple fabrication using only a single dielectric thin film. Although subwavelength features are required, nanoreplica molding approaches have been used to inexpensively produce devices over large surface areas with resonances encompassing the near UV to near-infrared (NIR) wavelengths.[17,18] These 1D surface structures generally exhibit narrowband coupling of normally incident light polarized in either the perpendicular or parallel to the direction of periodicity, where the period determines the resonant wavelength. A 2D surface structure, however, may be designed so that incident light polarized at orthogonal angles can encounter distinct periods, resulting in resonant reflection at wavelengths that can be chosen independently for each polarization.

A cross section and top-view schematic of such a structure is shown in Fig. 1. The device design is performed in consideration of a fabrication process utilizing a low refractive index polymer subwavelength periodic surface structure that is overcoated with a single thin film of high refractive index dielectric (TiO_2) as shown in Fig. 1(a). These devices are commonly referred to as PC slabs, and this nomenclature is used in this paper. The dimensions of the device are therefore constrained to a single grating depth (d) and TiO_2 thickness (t) for both EF and LF detection modes. To optimize the grating depth and TiO_2 thickness as well as the periods of the subwavelength structure in two lateral orthogonal directions, the resonance characteristics were modeled using rigorous coupled-wave analysis (RCWA). The simulation

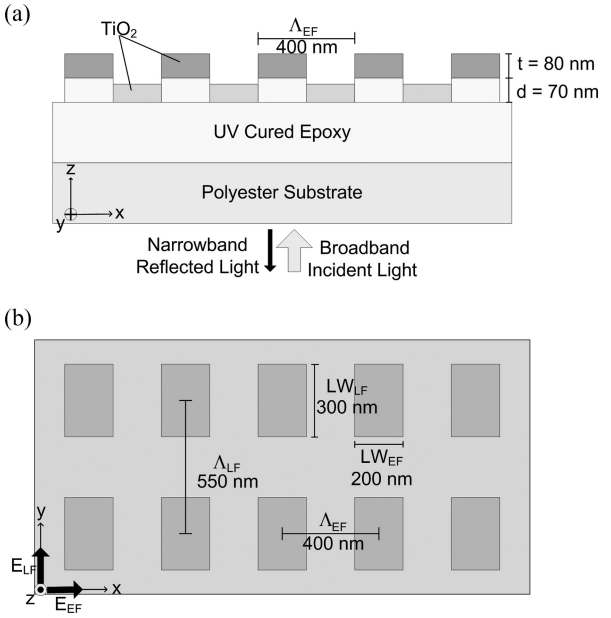

Fig. 1. Schematic of the optimized photonic crystal biosensor structure. Directional axes are noted on the bottom left of each structure. (a) Side view of the structure in the xz plane. The period in the EF direction, or Λ_{EF}, is 400 nm. The grating depth (d) is 70 nm, and the thickness of the TiO_2 layer (t) is 80 nm. The indices of refraction for the UV curable polymer and TiO_2 layers are 1.43 and 2.35, respectively. (b) Top-down view of the 2D structure. The electric field polarizations required to excite each mode of operation are noted on the coordinate axis. The periods in each direction are designated as Λ_{EF} and Λ_{LF}. The line widths associated with each period are noted by LW_{EF} and LW_{LF}.

was performed using eight harmonics in both the x and y directions. The period in the x direction (Λ_{EF}) and the period in the y direction (Λ_{LF}) were manipulated in addition to the grating depth and TiO_2 thickness, as the z direction is assumed to be the propagation direction of the illuminating light. The structure was modeled with known refractive indices (n) for the UV-curable epoxy substrate ($n = 1.43$) and sputtered TiO_2 ($n = 2.35$ at 635 nm). The device is attached to an ordinary glass microscope slide with the surface exposed to air during fluorescence measurements but with the surface exposed to an aqueous solution during LF measurement. Therefore for the design modeling, the background refractive index is set to $n = 1.0$ (air) for simulations at the EF wavelength, while the background refractive index is set to $n = 1.33$ (water) for simulations of LF detection.

Adjusting the resonant peak of one incoming light polarization to coincide with the excitation wavelength of the desired fluorophore is the foremost design consideration for the fluorescence enhancement mode of operation. In this case, 635 nm is the operating wavelength of the fluorescence scanner laser to be used in examining fluorescence from Cy5 bound to the sensor surface. In addition to tuning the wavelength of the peak, the behavior of the peak in response to changes in the angle of incident light must be moderated because it is not desirable for small angular changes in the incident light to drastically affect the fluorescence enhancement phenomenon. Thus the width of the resonant peak at the excitation wavelength must be broad as a function of the angle of incidence. The LF detection phenomenon also relies on creating a resonant peak reflection, but in the wavelength range for NIR spectral measurement as required by the LF detection instrumentation, which can detect a PC resonance in the 830–890 nm range. The LF detection modality relies on quantifying the PWV shift upon the adsorption of biomolecules to the sensor surface. The two important design parameters for sensitivity optimization of LF detection are the analyte's bulk refractive index shift coefficient ($S_b = \Delta\mathrm{PWV}/\Delta n$) and the spectral FWHM, or the width (in nanometers) of the resonant peak when the spectral lines are at half the value of the maximum reflected amplitude. The design must maximize the S_b to provide a larger signal for binding events and minimize the FWHM such that small changes in the PWV may be resolved. The design parameters were then selected to maximize the width of the EF peak as a function of incident angle and to minimize the FWHM of the LF peak while maintaining the necessary resonant wavelength values.

The desired sensor structure has $\Lambda_{EF} = 400$ nm, $\Lambda_{LF} = 550$ nm, a grating depth $d = 70$ nm, and a TiO_2 thickness $t = 80$ nm. The raised portion of the device structure in the y direction, or the LF direction line width (LW_{LF}), measures 300 nm, which is 55% of the period in that direction (Fig. 1). The differential coverage of TiO_2 between higher and lower portions of the grating and sidewall coverage was taken into account in determining these values. The resonant peak from light reflected by the structure is characterized primarily by PWV and FWHM of the zeroth-order diffracted wave in the direction of both periods. When this structure is modeled with the polarization of the incident wave along the direction of the EF period [E_{EF} polarization according to Fig. 1(b)], the reflected spectrum contains a peak with PWV of 635 nm and FWHM of 20 nm [Fig. 2(a)]. By measuring the reflection efficiency as a function of angle of incidence at an incident wavelength of 635 nm, the angular tolerance of the reflected peak was determined. This measurement suggests that the EF effect is observable over a wide range of angles centered at normal incidence, as the FWHM is approximately 3° [Fig. 2(b)]. The reflective properties of the device can be modeled for light in which the electric field component is parallel to the direction of the LF period as well [E_{LF} polarization according to Fig. 1(b)]. The simulated resonant peak from this illumination has a PWV at 853 nm and a FWHM of 8 nm [Fig. 2(c)]. For the E_{LF} polarization, $S_b = 140$ nm/RIU (refractive index units), indicating that a change of 0.01 RIU in the refractive index of the bulk solution would result in a 1.4 nm shift of the PWV. However, for the polarization in the EF direction, $S_b = 42$ nm/RIU, which suggests that the peak observed during illumination with E_{EF} polarized light will experience a signifi-

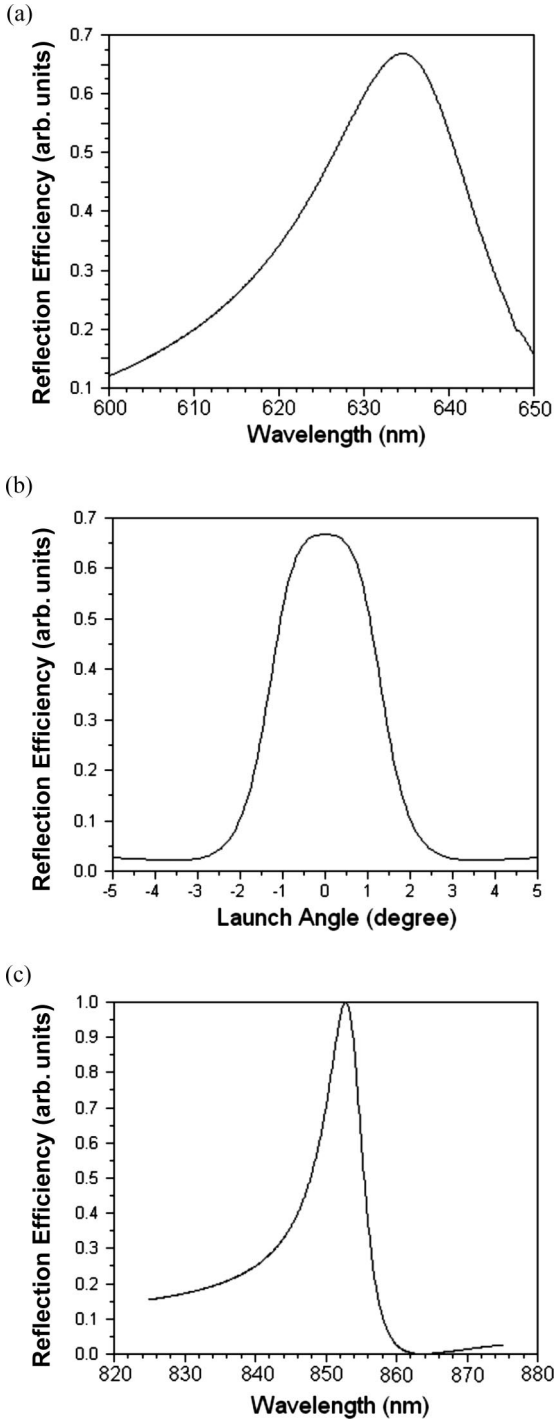

Fig. 2. Simulated reflection characteristics of device structure. (a) Reflection efficiency plotted as a function of wavelength for the polarization of light intended to excite the ER mode of operation with light at normal incidence. (b) Reflection efficiency plotted as a function of the variation of incidence angle from the surface normal. The light is polarized for ER excitation at a wavelength of 635 nm. (c) Reflection efficiency as a function of wavelength for the LF polarization of light.

cantly lower shift during protein adsorption than would be observed with the E_{LF} peak.

The electric near-field amplitude profile of the device is important in determining the EF performance

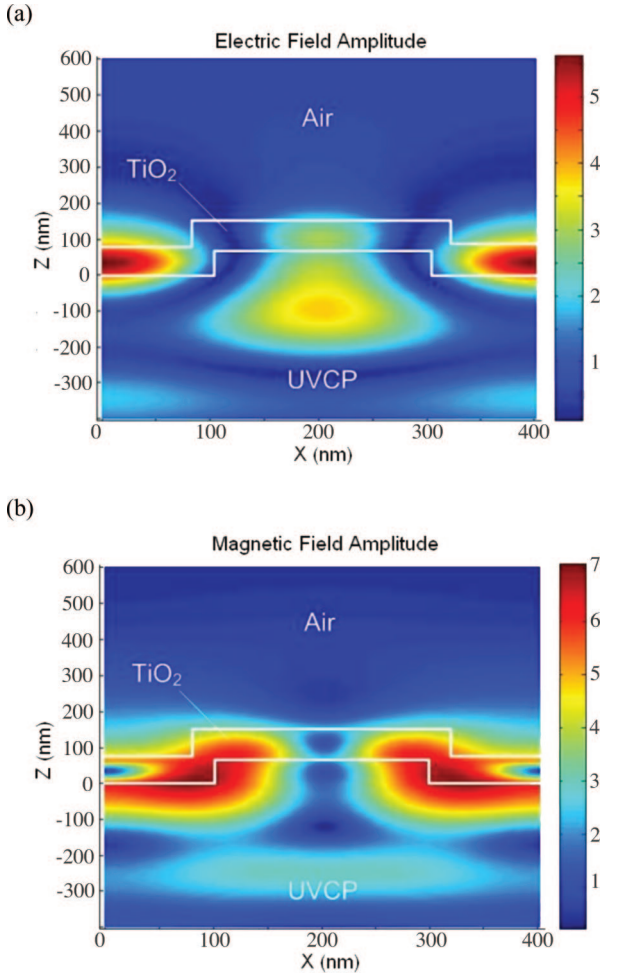

Fig. 3. Near-field profiles at a fixed y position (exactly in the center of the structure) for normally incident light of wavelength 635 nm polarized in the EF direction. The device structure is drawn into the figure and the layers of UV-curable polymer (UVCP), titanium dioxide (TiO_2), and air are noted. The amplitudes noted on the scale bar represent the combined field amplitude in all directions relative to the incident field amplitude. (a) Electric field profile. (b) Magnetic field profile.

and is plotted in the xz plane (cutting through the center of the structure) for a normally incident plane wave of E_{EF} polarization and wavelength 635 nm to simulate laser illumination (Fig. 3). The near-field amplitudes of the electric field in the x, y, and z directions are modeled by RCWA for this laser illumination condition and are normalized to the incident field amplitude (which sets the incident electric field amplitude in the EF direction to a value of 1). The amplitudes of electric field components in the x, y, and z directions are combined into a vector, from which the magnitude is calculated and plotted in Fig. 3(a). Likewise, the magnitude of the magnetic field can be calculated and appears in Fig. 3(b). The amplitudes in all three directions are combined because it is assumed that all components of the electric field are important to fluorophore excitation since the fluorophores will be randomly oriented on the device surface. As expected, the large-field amplification val-

ues are confined to within 100 nm of the sensor surface. The electric near-field amplitude profile can roughly be related to the fluorescence enhancement factor by calculating the square of the amplitude of the electric field, which is proportional to the fluorophore excitation rate,[19,20] which allows for calculation of the maximum expected enhancement by evaluating the square of the electric field amplitude at the surface of the structure. However, it is worth noting that the small number of harmonics used in the RCWA simulation (because of computational restrictions) likely gives only an estimate of the actual normalized electric field amplitude, but this estimate is indeed valuable in comparing the performance of different structures. An observation of Fig. 3(a) shows that the square of the normalized electric field at the device surface is approximately 20.

3. Materials and Methods

A. Device Fabrication

The fabrication of the device was carried out through a nanoreplica molding process, as described previously.[18] A direct-write electron-beam lithography process was utilized for fabrication of a master mold template on a silicon wafer. A layout of the desired 2D grating design was written onto a silicon substrate with a 200 nm oxide layer and a 950 K molecular weight poly(methylmethacrylate) (Microchem, Newton, Mass., USA) electron-beam resist masking layer by electron-beam lithography (Leica/Cambridge EBMF 10.5, Bannockburn, Ill., USA) over a 1 mm $\times$ 1 mm area. After electron-beam exposure, the substrate was developed in a 1:3 methyl isobutyl ketone:isopropyl alcohol solution. The SiO_2 layer was etched by a reactive ion etching in a CHF_3 plasma to a depth of 70 nm (Plasmalab Freon/O_2 Reactive Ion Etcher, Oxford Instruments, Concord, Mass., USA). The remainder of the masking layer was stripped by ultrasonication in a 1:1 methyl alcohol:methylene chloride solution.

The nanoreplica molding process that follows requires a transfer of the silicon master surface structure to a UV-curable polymer to produce the photonic crystal structure. The master was treated by immersion in dichlorodimethylsilane (PlusOne Repel Silane ES, GE Healthcare, Piscataway, N.J., USA) for 5 min to allow for release of UV-curable polymer after replication. Liquid polymer (Gelest, Inc., Morrisville, Pa., USA) was dispensed between the master and a thin sheet of poly(ethylene terepthalate) (PET), and was cured under a high-intensity ultraviolet lamp (Xenon) for 30 s. The replicated sensor structure was then lifted off from the master. Next, 80 nm of TiO_2 was deposited onto the sensor by sputtering (Cooke Dual Gun Sputter System, South Norwalk, Conn., USA). To determine the structural dimensions of the device, gold–palladium was sputtered onto some devices (SPI Au Sputter Coater, West Chester, Pa., USA), and these sensors were characterized with a scanning electron microscope (SEM, Hitachi 4800). The sensors to be tested for fluorescence enhancement and LF sensing were mounted onto standard microscope slides using an optically clear laminating adhesive.

B. Device Characterization

To determine the optical properties of the device, a reflection setup was used. Glass slides containing sensors were mounted on a custom holder and placed in the path of a collimated white-light source. The normally incident light was directed through a polarizer before reaching the slide holder, and the reflected spectrum was collected and fed into a spectrometer (Ocean Optics, Dunedin, Fla., USA). The transmitted spectrum as a function of angle was collected with a similar setup, except the device was mounted on an angular stage to allow rotation about a single axis, and light was transmitted through the device and collected.

C. Arraying

Sensors were functionalized by applying a high-density amine diluted in deionized water to the surface and incubating at 40 °C for 2 h. A solution of 25% glutaraldehyde in deionized water was then added to the sensors and incubated at room temperature for 2 h. Cy5-streptavidin (excitation at 650 nm, emission at 670 nm) at a concentration of 0.1 mg/ml was spotted on the sensors using a piezorray noncontact microarraying system (PerkinElmer, Waltham, Mass., USA). The dispensed liquid volume was set to 500 pL, and a square pattern of 36 spots with a 750 μm distance between the centers of the spots was generated by the system. Alignment of the initial spot to the sensor surface was achieved by manual calibration of the starting position. After arraying, the slide was incubated at 4 °C for 24 h.

D. Fluorescence Scanner

The fluorescence from Cy5-strepavidin on the surface of the sensor was quantified using an Axon GenePix 4000B microarray scanner. The scanner utilizes a 635 nm laser for excitation and an emission filter for measurement of light in the 650–690 nm range. Slides were scanned at a 5 μm resolution and a +200 μm focal plane because of the height of the PET layer above the glass slide surface. The photomultiplier tube (PMT) gain was adjusted upward or downward to prevent the signal from exceeding the maximum allowable PMT value at any pixel in the scan area.

E. Label-Free Detection Instrumentation

The sensor was scanned in an imaging instrument described previously.[9] The instrument measures the PWV across the sensor surface as a function of position in a pixel-by-pixel scan and constructs an image based on the PWV distribution. For this work, the imaging instrument was set to scan at a pixel size of 22.3 μm $\times$ 22.3 μm. Sensors were scanned before Cy5-streptavidin was arrayed on the surface and after the arraying process was complete. The PWV image obtained before the arraying procedure was

subtracted from the image after arraying so that the PWV shift from the adsorption of biomolecules on the sensor surface could be determined in the format of an image of the sensor.

4. Results

A. Device Fabrication

The electron-beam lithography process for creating the silicon master yielded a 1 mm × 1 mm area covered with a negative of the desired grating pattern. The resulting UV-curable polymer mold (without the addition of TiO_2) fabricated from this master has a period of 398 nm in the EF direction and 552 nm in the LF direction. The duty cycle, or ratio of the raised portion of the period to the total period, is 52% in the EF direction and 49% in the LF direction. After the addition of the 80 nm layer of TiO_2 by sputtering, the period is only slightly altered; the EF direction period is 397 nm and the LF direction period is 553 nm, with a maximum variation of less than 0.3% for both periods [Fig. 4(a)]. The addition of TiO_2, however, dramatically affects the duty cycle because of sidewall deposition from the sputtering process. The duty cycle of the final device becomes 62.0% in the EF direction and 62.7% in the LF direction, as the line widths increase by approximately 45 nm in both directions. This variation is partly accounted for in the computer model because TiO_2 sidewall coverage of approximately 20 nm on each edge of the post structure was included in the simulation. One obvious property of the fabricated PC structure that is not present in the computer model is the rounded profile of the post structures [Fig. 4(b)], which is caused by a lack of collimation during TiO_2 deposition. This discrepancy may cause some deviation of the observed sensor performance from that of the simulation characteristics.

B. Device Characterization

The measured reflection spectrum with air on the PC surface for light polarized for the EF operation is shown in Fig. 5(a). The PWV reflected from the device is 635 nm, and the FWHM is 13 nm. The simulation predicted the PWV to occur at the same wavelength and shows a FWHM that is 7 nm wider than the observed value. The observed reflected spectrum for light polarized for the LF mode of operation and with water on the PC surface is shown in Fig. 5(b). A PWV of 850 nm and a FWHM of approximately 15 nm is obtained, as compared with the simulated PWV of 852 nm and FWHM of 8 nm [Fig. 5(b)]. By placing isopropyl alcohol ($n = 1.38$) on the sensor surface, the

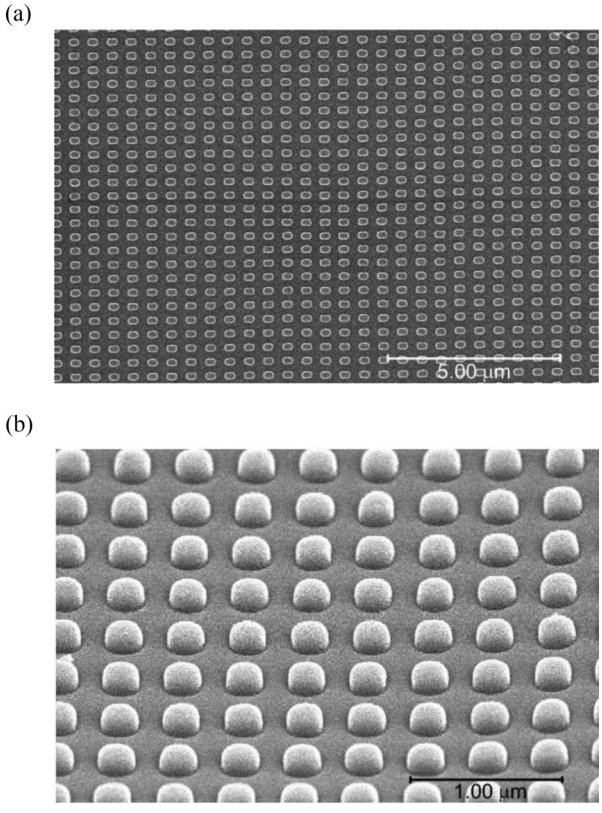

Fig. 4. SEM images of the final device structure. (a) Sensor structure viewed from directly above. The period in the ER direction (vertical) is 398 nm, and the period in the LF direction (horizontal) is 553 nm. The ER direction duty cycle is 62%, and the LF direction duty cycle is 63%. (b) Sensor structure viewed from a 30° angle. The structure profiles are significantly rounded due to the sputtering process.

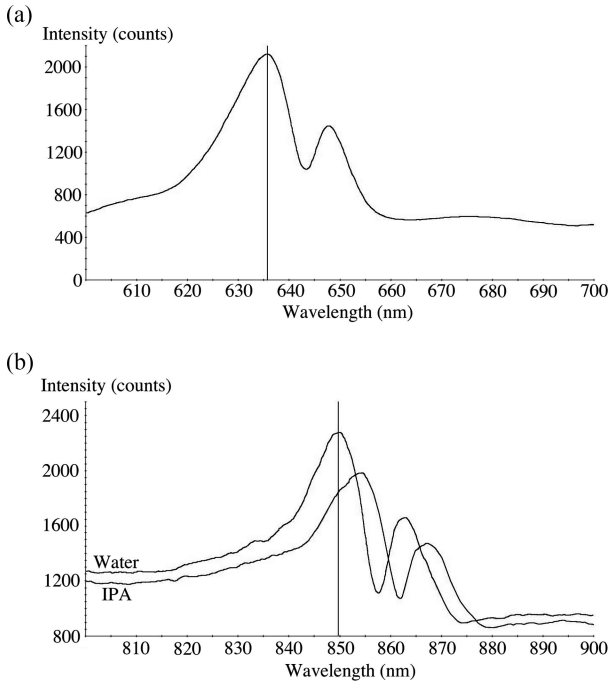

Fig. 5. Measured spectra after illumination with polarized, collimated white light. (a) Spectrum when illuminated with light polarized in the ER direction (simulation x direction). The resonant peak is centered at 635 nm with a FWHM of approximately 13 nm. (b) Spectra when illuminated with light polarized in the LF direction (simulation y direction) with water or isopropyl alcohol (IPA) as the bulk solutions. The sensor surface is immersed in water and displays a peak of PWV 850 nm and FWHM of approximately 15 nm under this condition. IPA is then applied to the sensor surface, resulting in a shift of approximately 4 nm.

mechanism of LF sensing is demonstrated, as the PWV of the reflected peak shifts to a higher wavelength due to the increase of bulk refractive index. The measured shift coefficient for the sensor, obtained by dividing the amount of wavelength shift by the refractive index change, is S_b = 90 nm/RIU, lower than the simulated value of 140 nm/RIU, indicating the LF sensitivity of the biosensor is 35% less sensitive than suggested by simulation.

Because the reflection characteristics are sensitive to the angle of the incident light, small changes in the incident angle of the light can result in one resonant peak splitting into two peaks of equal or lesser width. A further testing of the sensor structure revealed that the top plane of the replicated sensor surface was not perfectly parallel to the top plane of the microscope slide on which it was mounted. By adjusting the angle of incidence of the illumination light and measuring the transmitted spectra, this difference in the angle of normal incidence to the device structure as opposed to the microscope slide was approximately 0.5° for both polarizations and was likely caused by a bending of the plastic since it is stored in large rolls. This accounts for the reflection spectra for both wavelength ranges showing a secondary peak and for the smaller FWHM of the EF peak. Indeed, a simulation of illumination with this oblique incidence condition does show a split peak reflection is obtained, but the maximum field enhancement is identical when the lower of the two peaks occurs at 635 nm. Although the reflection spectra observed from the device can be obtained for light at normal incidence to the device structure, the microarray scanner and the imaging spectrometer illuminate the structure with light that is normally incident to the glass slide surface, making the spectra observed in Fig. 5 a more accurate representation of the resonant peaks excited during measurement with the sensor.

C. Fluorescence Enhancement by Photonic Crystal Enhanced Fluorescence

The image obtained by scanning the slide-mounted sensor in a commercial microarray scanner revealed significant fluorescent enhancement on the sensor surface. For a device with a resonant peak centered at 635 nm (after surface functionalization), the fluorescence intensity of a spot on the surface of the device was approximately 56,900 counts, while the average intensity for spots outside of the device was approximately 1600 counts (Fig. 6). This suggests a fluorescent enhancement factor of 35.6 times for regions in which the Cy5 dye is present. The fluorescence intensity in regions where no Cy5 is present is amplified as well, however, because of the enhancement of fluorescence in the UV curable polymer. The average intensity for those areas of the PC device without Cy5 is 680 counts, while a background signal of 200 counts is typically seen outside of the device structure. Despite the considerable increase in background signal exhibited by the photonic crystal, the signal-to-noise ratio (SNR), or the ratio of signal from fluorescent spots to the signal of the scanned surface

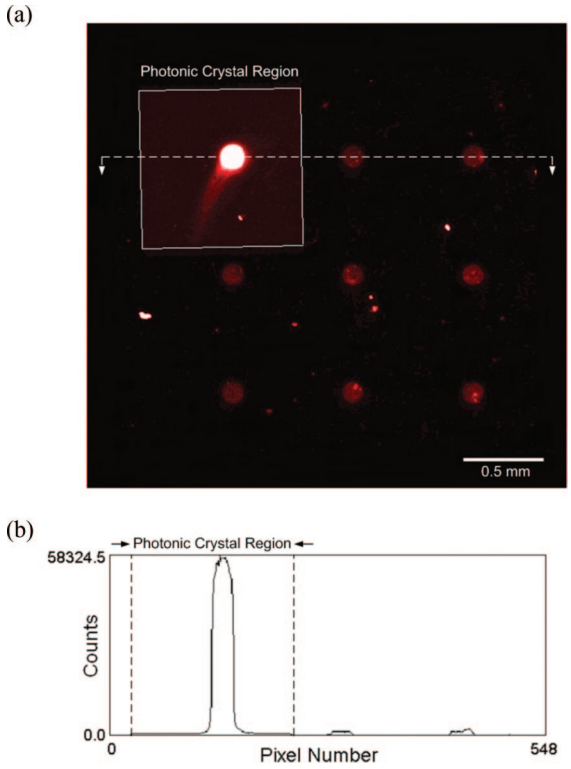

Fig. 6. (Color online) Fluorescence intensity data from Cy5-streptavidin spots on and off the device. (a) Fluorescence intensity image of data obtained from the microarray scan. Device scanned at 635 nm at a resolution of 5 μm. The photonic crystal region is labeled in addition to the line used to generate the image profile that appears in (b). (b) Image profile of spots on and off device, with the photonic crystal region labeled.

where no spots are present, is 1 order of magnitude higher for the PC surface than for the area without a surface structure; the SNR for fluorescence observed on the PC structure is 83.7, while this ratio is only eight times outside the grating structure. Although the spot profile on the PC is not significantly different than those spots off the PC, the spot present on the PC has a diameter of 155 μm, while the spots elsewhere have an average diameter of 130 μm. This is likely attributable to the fact that an aqueous solution can be retained between grating structures rather than drying completely before spotting. When the protein is spotted the added moisture promotes the diffusion over greater distances than would be seen on a flat layer of TiO_2.

D. Label-Free Detection of Analyte

By scanning the sensor with the LF detection imaging instrument before and after protein spotting, a spatial map of PWV shifts can be obtained within the resolution of the imaging spectrometer embedded in the instrument. The addition of 0.1 mg/ml streptavidin-Cy5 to the surface functionalized sensor resulted in a maximum PWV shift of 3.6 nm (Fig. 7). The spot displays noticeable nonuniformity, with the largest signal appearing at the center of the spot and decreasing toward the edges. According to

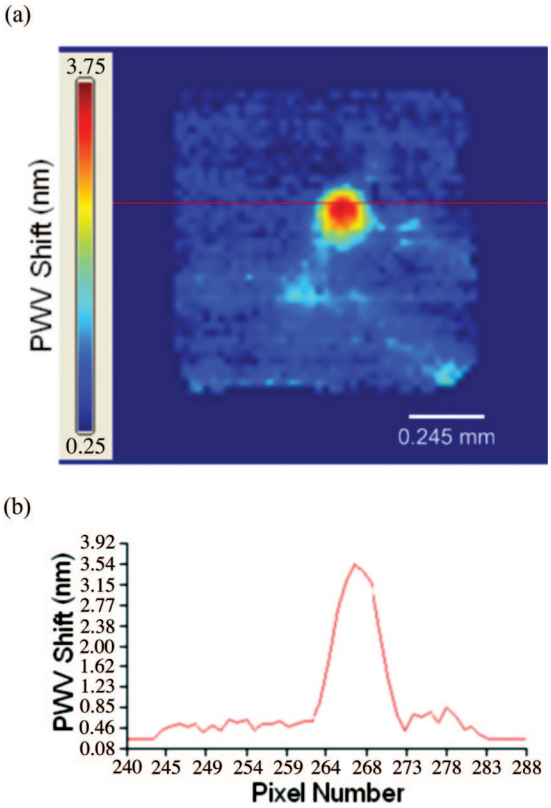

Fig. 7. Label-free detection data from Cy5-streptavidin spot on the device surface. (a) PWV shift image obtained from subtracting PWVs from a scan before spotting from those values from a scan after spotting. (b) Image profile of PWV shift values for one row of pixels through the center of the spot.

the LF scan, the spot has a diameter of 180 μm, which is considerably larger than the 155 μm diameter observed in the fluorescence image. However, the pixel size for the LF imaging instrument is 22.3 μm, as opposed to 5 μm for the fluorescence intensity measurement, so it would be expected that features may appear larger during the LF scan.

5. Discussion

The structure designed and tested in this work is to our knowledge the first demonstration of a 2D PC that can simultaneously enhance the fluorescent signal from a standard dye and perform LF adsorption detection on a single surface. Because this PC has a unique period in two orthogonal directions, resonant reflections can be obtained at two widely separated wavelengths simply by modulating the polarization of incident light. The fluorescence enhancement capabilities of this 2D PC structure, as measured by a conventional fluorescence scanner, are superior to previously demonstrated techniques on a microscope slide format,[3,21] yet this PC structure can perform LF detection as well. The LF detection sensitivity, as measured by the bulk refractive index shift coefficient, is only 20% lower than that of previously reported plastic-based 1D PC structures.[17] The FWHM of the LF resonance is also approximately four times wider, indicating that the LF detection of the 2D PC may suffer from poorer PWV shift resolution. This wider FWHM, however, is a result of tuning the design to achieve a larger FWHM in the EF resonance and was a design compromise made to ensure protein adsorption would not dramatically shift the entire EF peak away from the target wavelength. Despite these limitations, the LF detection assay performed in this work illustrates that the adsorption of a large protein to the glutaraldehyde surface chemistry produces a significant shift (approximately 3 nm).

While this PC is adequate in demonstrating a combined EF and LF biosensor, the performance of the device may be optimized further with regard to the LF detection performance. While the PWV observed experimentally with illumination of E_{LF} polarized light is nearly identical to that observed in simulation, the FWHM of the experimental peak is larger than the simulated peak, even after peak splitting (which is attributable to the slightly off-normal incidence of the illuminating light). In addition, the bulk shift coefficient S_b is approximately 30% lower than the simulated value. One factor that is likely responsible for the widening of the peak is the variation in the period throughout the device; a small percentage change of the period can lead to the PWV location shifting by a few nanometers. Other likely factors that may account for the discrepancy between simulated and experimental characteristics include an underestimation of the sidewall thickness in the simulated structure, significant rounding observed in the fabricated device, and deviations in the actual indices of refraction of materials from simulated values. Some of these issues may be resolved by decreasing the variation in period and employing a collimated deposition system for addition of the dielectric layer.

The EF mode of operation, on the other hand, performed better than expected. The FWHM of the peak during E_{EF} illumination is less than 70% of the predicted value, although this can be attributed to the split peak resulting from non-normal light incidence. Unexpectedly, however, the fluorescence enhancement is much higher than that predicted by simulation, even including the non-normal incidence illumination condition. A fluorescence enhancement of 35 times is observed, as opposed to the predicted factor of 20 times. Although the simulation is expected to provide only a rough estimate of the real enhancement factor, it is unlikely that this great increase in enhancement can be explained solely by small deviations of the RCWA model from reality. This increase in enhancement could be explained by enhanced extraction of light emitted by the fluorophores, as demonstrated previously in 2D PCs.[22] However, no data in this work can confirm or contradict this possibility, so it will be a subject of future study.

Owing to the constraints of our current electron-beam lithography process, the size of the 2D PC produced in this work was only 1 mm × 1 mm, a suitable size for only one or two protein spots. In future work, however, we plan to utilize projection lithography to produce a 2D PC silicon master of a large area to allow

incorporation of the structure into 1 in. × 3 in. microscope slides and 3 in. × 5 in. microplates. Adapting the sensor to these formats will allow assays to be carried out on multiple spots simultaneously. By using the nanoreplica molding approach to fabrication, the large-area PC structures can be produced inexpensively and attaching them to the glass slides and microplates currently used in life sciences research will ensure they are compatible with commercial fluorescence scanners and LF detection instrumentation.

The 2D PC structure described in this work, as with other previously demonstrated EF methodologies, has immediate applications in the field of DNA and protein microarrays. Fluorescence enhancement technologies have previously demonstrated lower thresholds for gene expression detection and higher SNRs than conventional microarrays.[3,21] Because this PC structure retains the EF capabilities while allowing for independent LF measurements of adsorption, it is a more versatile tool than similar EF techniques. The LF detection mode may be applied to oligonucleotide or protein spots in the prehybridization stage of an experiment to map spot profiles, allowing for fluorescence independent measurements for spot quality control; current methods of spot quality assessment rely on one or more extra labeling steps and additional fluorescence measurements.[23,24] Using both modes of this PC structure also enables the correlation of fluorescent signals to quantitative ligand densities as measured by LF detection, which may assist in the comparison of the binding properties of spots containing different types of biomolecules.

This PC also has potential applications in the area of cell-based assays, which are an emerging tool for pharmaceutical drug compound screening because they assess the impact compounds may have *in vivo* more accurately than typical ligand-binding assays.[25] Fluorescence imaging plate readers can be utilized for assessments of cell ion channel function when performing high-throughput screening for ion channel-targeting drugs[26,27] and for measuring cardiotoxic responses to drugs in a high-throughput fashion.[28] The SNR (ratio of fluorescent molecule signal to background signal) of microplate fluorescence assays of ion channel function (and for the presence of other cell membrane proteins) can be improved dramatically by the incorporation of this PC surface in microplates since it enhances fluorescence only within 100–200 mm of the structure surface. The LF mode of operation would simultaneously allow for an independent measurement of cell attachment to the PC surface, which can be incorporated with fluorescence measurements to further improve the SNR. LF cell-based assays have previously been demonstrated with a PC biosensor to observe the cytotoxic effects of compounds and to monitor the presence of specific cell surface proteins.[29] By incorporating these LF assays with fluorescence assays utilizing EF, one can perform experiments to evaluate the effect of drug compound candidates on cell function, particularly on cell surface protein function and cell viability in a highly sensitive fashion.

The design methodology utilized in this work is not limited to designing combined enhanced fluorescence and LF adsorption detection sensors but can also be followed to create PC structures capable of promoting EF at two distinct wavelengths. Because observation of the EF phenomenon is dependent on the wavelength of resonant peaks, which can be adjusted by modulation of a small number of PC dimensions, an EF device can be made for any two fluorescent dyes. The NIR resonant peak of the device used in this work could be used for the EF of a dye fluorescing in NIR wavelengths rather than LF adsorption detection if desired. Alternately, another PC could be designed to form a resonant peak at another visible wavelength rather than at a NIR wavelength. Thus a PC capable of enhancing fluorescence from both Cy5 and Cy3 dyes could be created to improve the sensitivity and SNR of standard dual dye DNA microarrays currently performed by many biologists.

6. Conclusion

A 2D PC surface structure has been designed and fabricated for LF detection and enhanced fluorescence detection, where orthogonal light polarizations are used to excite resonances corresponding to each of the independent detection modalities that are designed to operate at different wavelengths. The 2D PC resonance behavior, field enhancement, and LF sensitivity were accurately predicted by a RCWA computer model, and images of adsorbed biomolecule spots were obtained by a conventional fluorescence laser scanner and by a LF imaging instruement. In a scaled-up format, enabled by the inexpensive nanoreplica molding fabrication technique, this PC structure is expected to find applications in genomics, proteomics, and cell-based assays.

The authors acknowledge funding from the National Science Foundation (BES0427657) and SRU Biosystems. The authors thank the W. M. Keck Center for Comparative and Functional Genomics for access to its microarray scanner. The authors also thank the staff of the Micro and Nanotechnology Laboratory and colleagues from the Nano Sensors Group for their suggestions and input. Any opinions, findings, and conclusions or recommendations expressed in this material are those of the authors and do not necessarily reflect the views of the National Science Foundation.

References

1. M. Schena, D. Shalon, R. W. Davis, and P. O. Brown, "Quantitative monitoring of gene expression patterns with a complementary DNA microarray," Science **270,** 467–470 (1995).
2. A. Q. Emili and G. Cagney, "Large-scale functional analysis using peptide or protein arrays," Nat. Biotechnol. **18,** 393–397 (2000).
3. W. Budach, D. Neuschafer, C. Wanke, and S.-D. Chibout, "Generation of transducers for fluorescence-based microarrays with enhanced sensitivity and their application for gene expression profiling," Anal. Chem. **75,** 2571–2577 (2003).

4. D. Neuschafer, W. Budach, C. Wanke, and S.-D. Chibout, "Evanescent resonator chips: a universal platform with superior sensitivity for fluorescence-based microarrays," Biosens. Bioelectron. **18,** 489–497 (2003).
5. J. Homola, S. S. Yee, and G. Gauglitz, "Surface plasmon resonance sensors: review," Sens. Actuators B **54,** 3–15 (1999).
6. B. Liedberg, C. Nylander, and I. Lundstrom, "Surface plasmon resonance for gas detection and biosensing," Sens. Actuators **4,** 299–304 (1983).
7. S. Lofas, M. Malmqvist, I. Ronnberg, E. Stenberg, B. Liedberg, and I. Lundstrom, "Bioanalysis with surface plasmon resonance," Sens. Actuators B **5,** 79–84 (1991).
8. W. Huber, R. Barner, C. Fattinger, J. Hubscher, H. Koller, F. Muller, D. Schlatter, and W. Lukosz, "Direct optical immunosensing (sensitivity and selectivity)," Sens. Actuators B **6,** 122–126 (1992).
9. P. Y. Li, B. Lin, J. Gerstenmaier, and B. T. Cunningham, "A new method for label-free imaging of biomolecular interactions," Sens. Actuators B **99,** 6–13 (2004).
10. B. Cunningham, P. Li, B. Lin, and J. Pepper, "Colorimetric resonant reflection as a direct biochemical assay technique," Sens. Actuators B **81,** 316–328 (2002).
11. S. S. Wang, R. Magnusson, J. S. Bagby, and M. G. Moharam, "Guided-mode resonances in planar dielectric-layer diffraction gratings," J. Opt. Soc. Am. A **7,** 1470–1474 (1990).
12. R. Magnusson and S. S. Wang, "New principle for optical filters," Appl. Phys. Lett. **61,** 1022–1024 (1992).
13. Y. Ding and R. Magnusson, "Resonant leaky-mode spectral-band engineering and device applications," Opt. Exp. **12,** 5661–5674 (2004).
14. C. Wei, S. Liu, D. Deng, J. Shen, J. Shao, and Z. Fan, "Electric field enhancement in guided-mode resonance filters," Opt. Lett. **31,** 1223–1225 (2006).
15. R. Magnusson, D. Shin, and Z. S. Liu, "Guided-mode resonance Brewster filter," Opt. Lett. **23,** 612–614 (1998).
16. Z. S. Liu, S. Tibuleac, D. Shin, P. P. Young, and R. Magnusson, "High-efficiency guided-mode resonance filter," Opt. Lett. **23,** 1556–1558 (1998).
17. B. Cunningham, B. Lin, J. Qiu, P. Li, J. Pepper, and B. Hugh, "A plastic colorimetric resonant optical biosensor for multiparallel detection of label-free biochemical interactions," Sens. Actuators B **85,** 219–226 (2002).
18. N. Ganesh and B. T. Cunningham, "Photonic-crystal near-ultraviolet reflectance filters fabricated by nanoreplica molding," Appl. Phys. Lett. **88,** 071110–071113 (2006).
19. D. A. Weitz, S. Garoff, J. I. Gersten, and A. Nitzan, "The enhancement of Raman scattering, resonance Raman scattering, and fluorescence from molecules adsorbed on a rough silver surface," J. Chem. Phys. **78,** 5324–5338 (1983).
20. P. Anger, P. Bharadwaj, and L. Novotny, "Enhancement and quenching of single-molecule fluorescence," Phys. Rev. Lett. **96,** 113002 (2006).
21. H. Choumane, N. Ha, C. Nelep, A. Chardon, G. O. Reymond, C. Goutel, G. Cerovic, F. Vallet, C. Weisbuch, and H. Bensity, "Double interference fluorescence enhancement from reflective slides: Application to bicolor microarrays," Appl. Phys. Lett. **87,** 031102 (2005).
22. M. Boroditsky, R. Vrijen, T. F. Krauss, R. Coccioli, R. Bhat, and E. Yablonovitch, "Spontaneous emission extraction and Purcell enhancement from thin-film 2D photonic crystals," J. Lightwave Technol. **17,** 2096–2112 (1999).
23. J. R. Shearstone, N. E. Allaire, M. E. Getman, and S. Perrin, "Nondestructive quality control for microarray production," BioTechniques **32,** 1051–1057 (2002).
24. X. Wang, N. Jiang, X. Feng, Y. Xie, P. J. Tonellato, S. Ghosh, and M. J. Hessner, "A novel approach for high-quality microarray processing using third-dye array visualization technology," IEEE Trans. Nanobiosc. **2,** 193–201 (2003).
25. G. E. Croston, "Functional cell-based uHTS in chemical genomic drug discovery," Trends Biotechnol. **20,** 110–115 (2002).
26. J. Denyer, J. Worley, B. Cox, G. Allenby, and M. Banks, "HTS approaches to voltage-gated ion channel drug discovery," Drug Discovery Today **3,** 323–332 (1998).
27. J. E. Gonzalez, K. Oades, Y. Leychkis, A. Harootunian, and P. A. Negulescu, "Cell-based assays and instrumentation for screening ion-channel targets," Drug Discovery Today **4,** 431–439 (1999).
28. R. Netzer, A. Ebneth, U. Bischoff, and O. Pongs, "Screening lead compounds for QT interval prolongation," Drug Discovery Today **6,** 78–84 (2001).
29. B. T. Cunningham, P. Li, S. Schulz, B. Lin, C. Baird, J. Gerstenmaier, C. Genick, F. Wang, E. Fine, and L. Laing, "Label-free assays on the BIND system," J. Biomol. Screening **9,** 481–490 (2004).